nature nanotechnology

ARTICLES

PUBLISHED ONLINE: 23 FEBRUARY 2014 | DOI: 10.1038/NNANO.2014.16

Electrical detection of charge-current-induced spin polarization due to spin-momentum locking in Bi_2Se_3

C. H. Li[1]*, O. M. J. van 't Erve[1], J. T. Robinson[2], Y. Liu[3], L. Li[3] and B. T. Jonker[1]*

Topological insulators exhibit metallic surface states populated by massless Dirac fermions with spin-momentum locking, where the carrier spin lies in-plane, locked at right angles to the carrier momentum. Here, we show that a charge current produces a net spin polarization via spin-momentum locking in Bi_2Se_3 films, and this polarization is directly manifested as a voltage on a ferromagnetic contact. This voltage is proportional to the projection of the spin polarization onto the contact magnetization, is determined by the direction and magnitude of the charge current, scales inversely with Bi_2Se_3 film thickness, and its sign is that expected from spin-momentum locking rather than Rashba effects. Similar data are obtained for two different ferromagnetic contacts, demonstrating that these behaviours are independent of the details of the ferromagnetic contact. These results demonstrate direct electrical access to the topological insulators' surface-state spin system and enable utilization of its remarkable properties for future technological applications.

Topological insulators (TIs) form a new quantum phase of matter distinct from the classic dichotomy of metals and semiconductors[1–4]. Whereas the bulk states form a bandgap, the surface states form a Dirac cone similar to graphene (Fig. 1a) and are topologically protected against disorder scattering. In marked contrast with the spin-degenerate bands of graphene, TI surface states are spin polarized. Topological insulators are expected to produce new functionalities[5] and enable insights into complex phenomena in many scientific arenas including spintronics[6–8], quantum information technology[9], highly correlated electron systems[10], magnetic monopoles[11] and quantized magnetoelectric coupling[12]. Examples of TI materials include $Bi_{1-x}Sb_x$ (ref. 4), Bi_2Se_3, Bi_2Te_3 and Sb_2Te_3 (refs 13–15).

One of the most striking properties is spin-momentum locking; the spin of the TI Dirac surface state lies in-plane, and is locked at right angles to the carrier momentum. An unpolarized charge current should thus create a net spin polarization, the amplitude and orientation of which are controlled by the charge current. This remarkable property has been anticipated by theory[16–18], but never accessed in a simple transport structure. A top view of a cross-section of the surface-state bands taken above the Dirac point is approximately circular (with slight hexagonal warping[19]), with the spin tangential at all points, as shown by the solid line in Fig. 1b. A net momentum along the k_x direction (represented by a displacement of this circular cross-section along k_x, indicated by the dashed circle) produced by an electric field results in an electron current I_e along x. Owing to spin-momentum locking, this simultaneously induces a spin current with a spin polarization oriented along $-y$. Thus, an unpolarized surface-state charge current creates a net spin polarization, with amplitude and orientation determined by the amplitude and direction of the charge current (Fig. 1c). Spin-momentum locking has been probed by spin-resolved photoemission[14,20,21] and polarized optical spectroscopic techniques[22], but never accessed in a simple transport geometry.

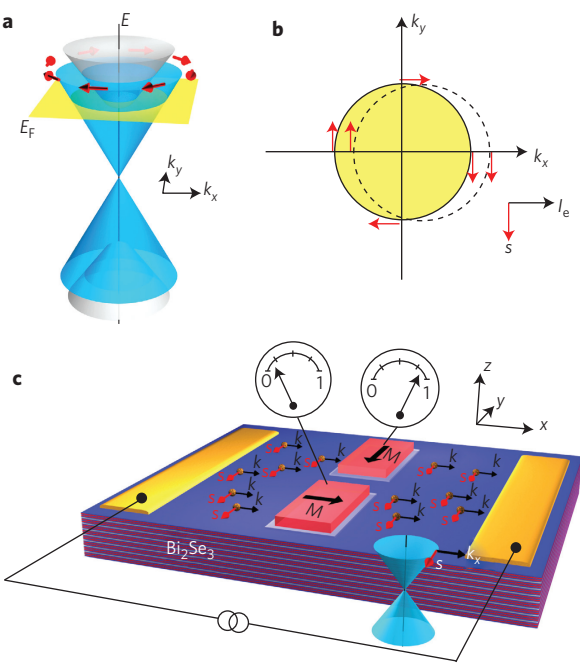

Figure 1 | Schematic of TI surface bands and experimental concept. **a**, Dirac cone of the TI surface states (blue), with the spin at right angles to the momentum at each point. The bulk conduction and valence bands are shown in grey. **b**, Top view of a slice in the k_x-k_y plane of the TI surface states. An applied voltage produces a net momentum along k_x and spin-momentum locking gives rise to a net spin polarization oriented in-plane and at right angles to the current. **c**, Concept drawing of the transport experiment. The voltage measured at the ferromagnetic detector is proportional to the projection of the current-induced TI spin polarization onto the contact magnetization.

[1]Materials Science and Technology Division, Naval Research Laboratory, Washington, District of Columbia 20375, USA, [2]Electronics Science and Technology Division, Naval Research Laboratory, Washington, District of Columbia 20375, USA, [3]Department of Physics, University of Wisconsin, Milwaukee, Wisconsin 53211, USA. *e-mail: connie.li@nrl.navy.mil; berry.jonker@nrl.navy.mil

Report Documentation Page

Form Approved
OMB No. 0704-0188

1. REPORT DATE	2. REPORT TYPE	3. DATES COVERED
2014		**00-00-2014 to 00-00-2014**

4. TITLE AND SUBTITLE	5a. CONTRACT NUMBER
Electrical detection of charge-current-induced spin polarization due to spin-momentum locking in Bi2Se3	5b. GRANT NUMBER
	5c. PROGRAM ELEMENT NUMBER
6. AUTHOR(S)	5d. PROJECT NUMBER
	5e. TASK NUMBER
	5f. WORK UNIT NUMBER
7. PERFORMING ORGANIZATION NAME(S) AND ADDRESS(ES) **Materials Science and Technology Division, Naval Research Laboratory,Naval Research Laboratory,Washington,DC,20375**	8. PERFORMING ORGANIZATION REPORT NUMBER
9. SPONSORING/MONITORING AGENCY NAME(S) AND ADDRESS(ES)	10. SPONSOR/MONITOR'S ACRONYM(S)
	11. SPONSOR/MONITOR'S REPORT NUMBER(S)

12. DISTRIBUTION/AVAILABILITY STATEMENT
Approved for public release; distribution unlimited

13. SUPPLEMENTARY NOTES
NATURE NANOTECHNOLOGY,2014

14. ABSTRACT

15. SUBJECT TERMS

16. SECURITY CLASSIFICATION OF:			17. LIMITATION OF ABSTRACT	18. NUMBER OF PAGES	19a. NAME OF RESPONSIBLE PERSON
a. REPORT	b. ABSTRACT	c. THIS PAGE			
unclassified	**unclassified**	**unclassified**	**Same as Report (SAR)**	**8**	

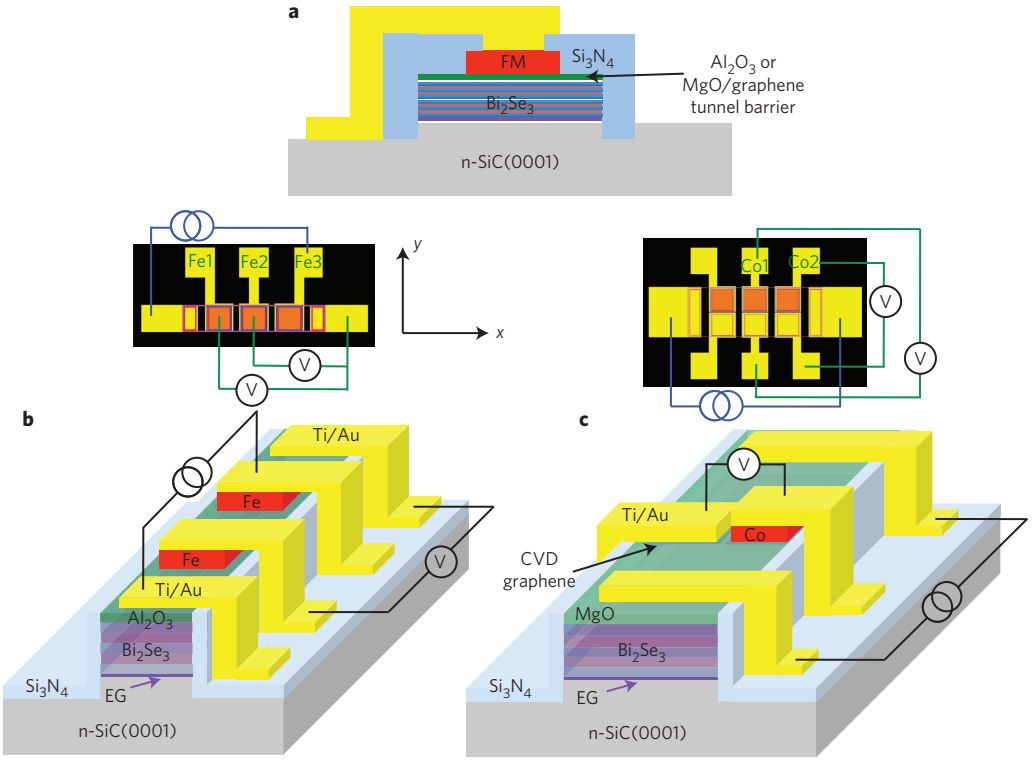

Figure 2 | Schematic of contacts and transport devices. a, Cross-section of a typical ferromagnetic contact. **b**, Top view of contact layout for devices with a single row of collinear ferromagnetic detector contacts (solid red) and coordinate axes. The ferromagnetic contacts have dimensions of 80 × 80 μm separated by 45 μm, edge to edge. The representative cross-section does not show all of the contacts, for clarity. **c**, As in **b**, but for devices with two parallel rows of collinear detector contacts: top row is ferromagnetic (solid red); bottom row is a non-magnetic reference. The ferromagnetic contacts have dimensions of either 80 × 80 μm or 60 × 60 μm, separated by 45 μm and 40 μm edge to edge, respectively. An adjacent parallel row of non-magnetic reference contacts (Au/Ti) of the same dimensions is separated from the ferromagnetic contacts by 15 μm, edge to edge. The representative cross-section does not show all of the contacts for clarity.

Here, we show direct electrical detection of the bias current-induced spin polarization as a voltage measured on a ferromagnetic metal tunnel barrier surface contact. The magnetization of the contact determines the spin detection axis, and the voltage measured at this contact is proportional to the projection of the TI spin polarization onto this axis. Although high bulk carrier densities provide a parallel bulk conduction channel, we observe dependencies on experimental parameters that are most straightforwardly explained by spin-momentum locking in surface states. An unpolarized bias current is applied between two non-magnetic contacts. When the charge current is orthogonal to the magnetization of the ferromagnetic detector contact, the TI spin is parallel (or antiparallel) to the magnetization, as shown in Fig. 1c, and a spin-related signal is detected at the ferromagnetic contact proportional to the magnitude of the charge current. When the direction of the charge current is reversed, the measured voltage changes sign. As the contact magnetization is reversed by applying a small in-plane magnetic field, the measured spin voltage mirrors the hysteresis loop of the contact. When the contact magnetization is rotated in-plane 90° so that the charge current is parallel to the magnetization, no spin voltage is detected, because the TI spin polarization is now orthogonal to the contact magnetization. The voltage measured scales inversely with Bi_2Se_3 film thickness and its sign is that expected from spin-momentum locking and opposite that of a Rashba effect. Similar data are obtained for two different ferromagnetic contact structures, Fe/Al_2O_3 and Co/MgO/graphene, underscoring the fact that these behaviours are due to bias current-induced spin polarization in the TI surface states rather than the bulk and are independent of the details of the contact. These results demonstrate simple and direct electrical access to the TI Dirac surface-state spin system and provide clear evidence for the spin-momentum locking and bias current-induced spin polarization. These results also identify a pathway for future experiments and enable utilization of TI properties for technological applications[5–8].

Bi_2Se_3 is regarded as a model TI. It exhibits a single Dirac cone and the largest bandgap (~0.3 eV) of known TIs[13], and its topological surface states have been shown to persist to at least room temperature due to weak electron–phonon coupling[14,23]. Recent work has shown that these topologically protected surface states are remarkably insensitive to both magnetic and non-magnetic surface adsorbates[24,25] and maintain their linear dispersion even when forming a planar interface with Fe_7Se_8, a ferromagnet with in-plane magnetization[26]. Those authors also found little solubility of Fe into the Bi_2Se_3 (ref. 26), and the studies did not address spin polarization. Spin-resolved photoemission on ferromagnetic ternary alloys with a magnetic dopant, $Bi_{2-x}Mn_xSe_3$ ($x \leq 0.1$), showed dramatic effects on spin texture near the Dirac point, but little at higher energies[27]. Such robustness is essential for the realization of future device structures based on the interplay of spin transport, ferromagnetism and spin-momentum locking.

Bi_2Se_3(111) films 11–45 nm thick were grown by molecular beam epitaxy (MBE) on epitaxial graphene (EG)/SiC(0001) and Al_2O_3(0001) at substrate temperatures of 275–325 °C (see Methods). The as-grown films were n-type with a net carrier density of $n \approx 1 \times 10^{19}$ cm^{-3} so that the Fermi level was within the bulk conduction band.

Two types of ferromagnetic detector contact were used—Fe/Al_2O_3 and Co/MgO/graphene (see Methods)—and similar

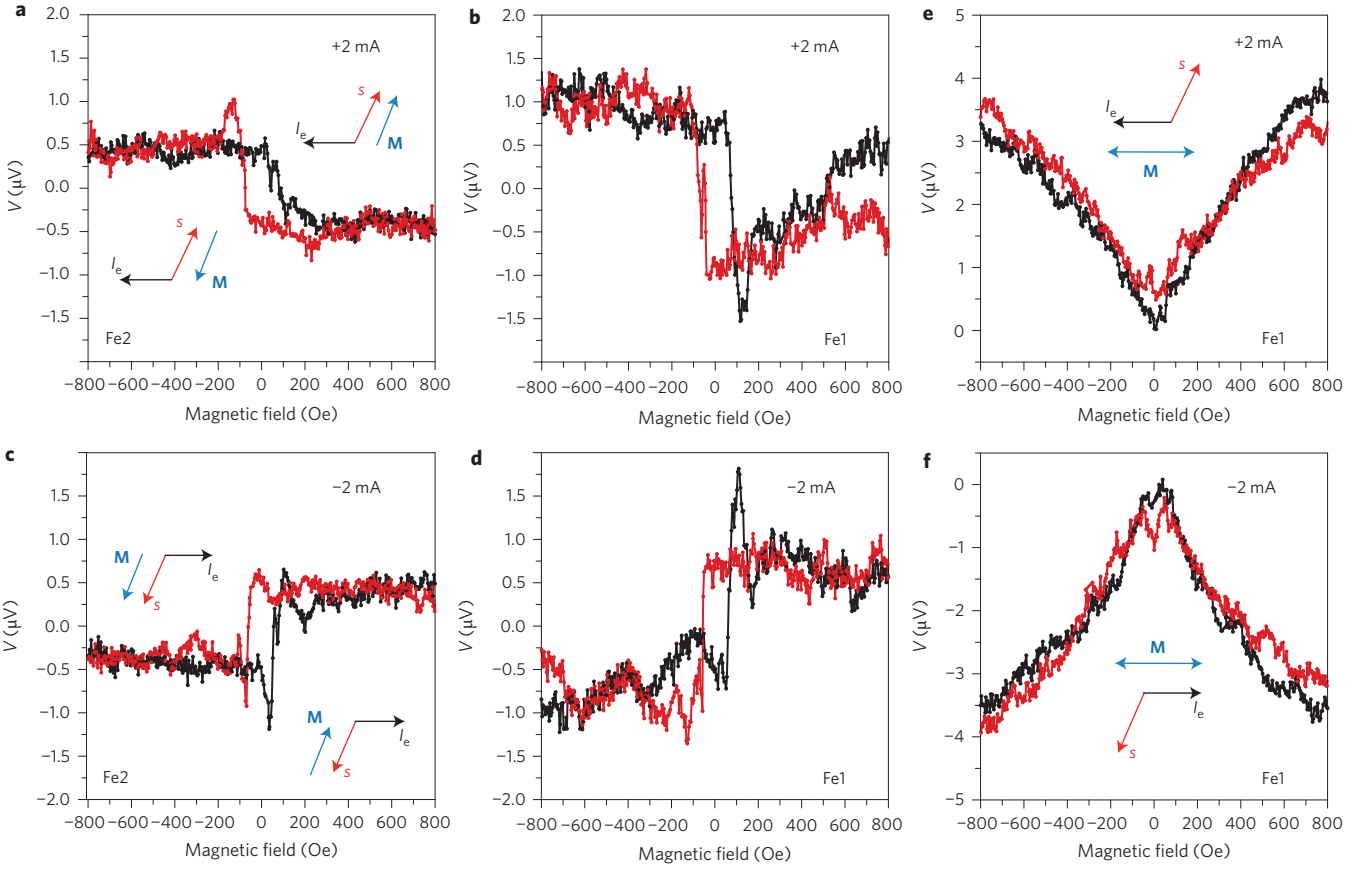

Figure 3 | TI spin polarization detected as a voltage with Fe/Al_2O_3 contacts. The contact layout of Fig. 2b is used and the Bi_2Se_3 film is 45 nm thick. **a**,**c**, Field dependence of the voltage measured using contact Fe2 as the detector with the magnetization collinear with the induced TI spin for bias currents of +2 mA and −2 mA, respectively. **b**,**d**, Similar data for contact Fe1 as the detector. **e**,**f**, Field dependence of the voltage measured using contact Fe1 as the detector with the magnetization orthogonal to the induced TI spin for bias currents of +2 mA and −2 mA, respectively. Black traces correspond to positive magnetic field sweeps (from negative to positive values) and red traces correspond to negative field sweeps. The relative orientations of I_e, induced TI spin polarization *s* and detector magnetization **M** are shown in the insets. All data were obtained at $T = 8$ K.

results were obtained for each. Such contacts have successfully enabled electrical detection of spin current and accumulation in other material systems[28] and their application to TIs has recently been treated theoretically[29]. The oxide layers ensure that no direct magnetic exchange interaction occurs between the ferromagnetic metal and TI surface states. The samples were processed into the device structures presented in Fig. 2, which consist of a co-linear series of ferromagnetic detector and non-magnetic Au/Ti reference contacts, with adjacent contacts separated by 40–45 μm. The magnetic characteristics of the ferromagnetic contacts were determined from anisotropic magnetoresistance measurements, as described in the Supplementary Section 'Ferromagnetic contacts'. The Fe contacts exhibited square magnetization versus applied field loops with a coercive field of 62 ± 5 Oe. The Co contacts exhibited slightly skewed loops with much higher coercive fields of 150 ± 5 Oe.

To probe the current-induced spin polarization of the TI surface states, measurements were performed with an Fe/Al_2O_3 contact as a detector on a 45-nm-thick Bi_2Se_3 film, using the contact layout shown in Fig. 2b. A fixed bias current flows between two other contacts on either side of and co-linear with the detector. The voltage at the detector was recorded with a high-impedance voltmeter (>1 GΩ) as a function of an in-plane magnetic field applied either parallel or orthogonal to the electron bias current direction in the TI. No current flows through the detector contact. A linear background was subtracted and the data centred on the vertical axis. An example of the raw data and background subtraction are shown in the Supplementary Section 'Raw data and background subtraction'. Electrons flow from left to right along the $+x$ axis for a negative bias current and a positive magnetic field points in either the $+x$ or $+y$ direction.

When the magnetic field is applied orthogonal to the current direction, the detector contact magnetization is switched to be either parallel or antiparallel to the current-induced spin in the TI surface (Fig. 1c) and the detector voltage exhibits clear hysteretic behaviour, as shown in Fig. 3a for contact Fe2. The relative orientation of I_e, induced TI spin polarization *s* and contact magnetization *M* are shown in the insets. At large positive fields, the magnetization is parallel to the TI surface-state spin polarization, and a constant negative voltage is measured as the magnetic field decreases to zero. As the magnetic field changes to small negative values (red trace), an abrupt increase in detector voltage is observed at the coercive field (−65 Oe) of the detector, that is, when the detector magnetization reverses to be antiparallel with the TI surface-state spin. Further ramping the magnetic field to −800 Oe produces little change in the detector voltage, and the overall scan exhibits a single step-like behaviour. When the field sweep direction is reversed so that it increases from negative to positive values (black trace), the detector voltage is constant until the positive coercive field of +65 Oe is reached. At this point, the voltage abruptly decreases as the contact magnetization again switches and becomes parallel with the spin orientation of the TI surface state. Similar step-like behaviour is observed at an adjacent detector contact labelled Fe1, as seen in Fig. 3b.

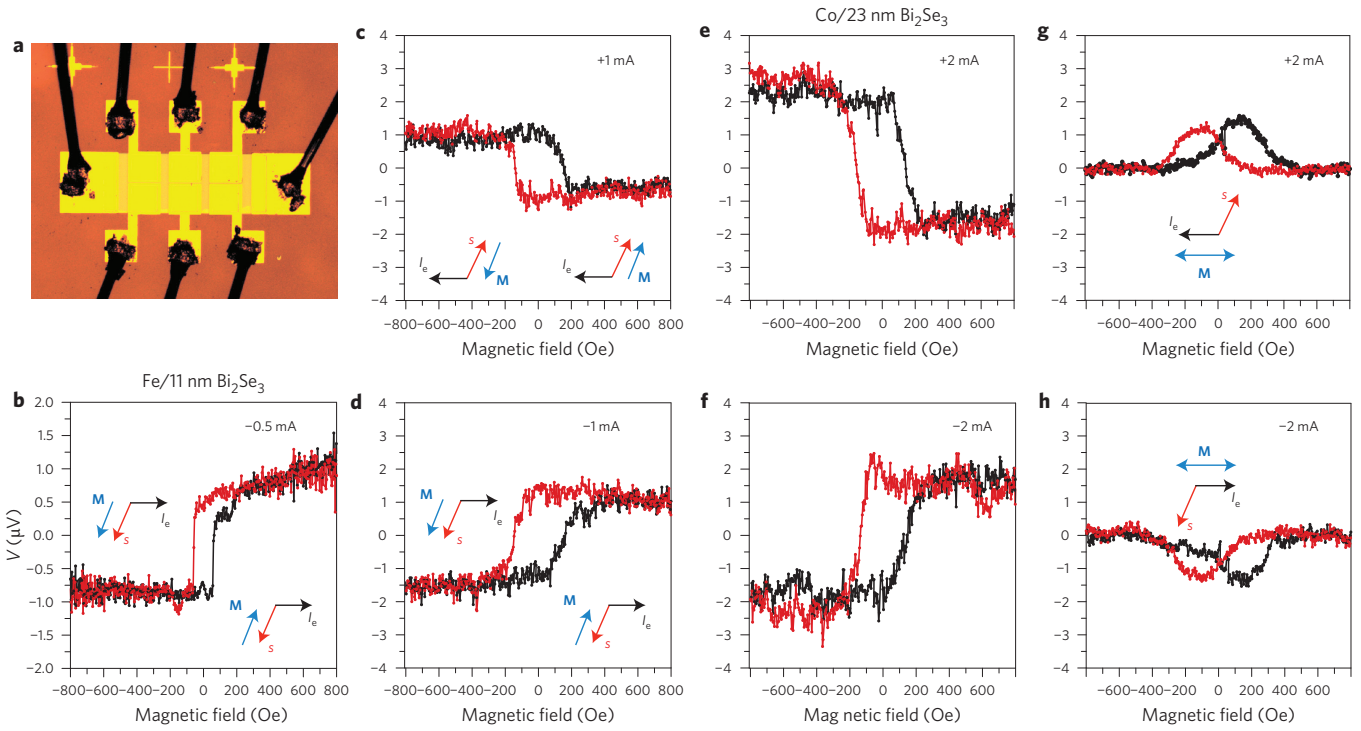

Figure 4 | TI spin polarization detected as a voltage with Fe/Al_2O_3 and Co/MgO/graphene contacts. The contact layout of Fig. 2c is used for two Bi_2Se_3 film thicknesses. **a**, Optical image of one of the devices measured. The bond pads near the bottom of the figure have dimensions of 100 × 100 μm. **b**, Magnetic field dependence of the voltage measured using Fe/Al_2O_3 tunnel barrier detectors on an 11-nm-thick Bi_2Se_3 film with the magnetization collinear with the induced TI spin for a bias current of -0.5 mA. **c**–**f**, As in **b**, but with Co/MgO/graphene detectors on a 23-nm-thick Bi_2Se_3 film for bias currents of +1 mA (**c**), −1 mA (**d**), +2 mA (**e**) and −2 mA (**f**). **g**,**h**, Field dependence of the voltage measured with the Co detector magnetization orthogonal to the induced TI spin for bias currents of +2 mA and -2 mA, respectively. The detector contacts have areas of 80 × 80 μm and all data were obtained at $T = 8$ K. Black traces correspond to positive magnetic field sweeps (from negative to positive values) and red traces correspond to negative field sweeps. The *y* axis label, $V(\mu V)$, is the same for all panels.

When the direction of the bias current is reversed, the orientation of the TI spin is also reversed and the field dependence of the FM detector voltage flips about the zero-voltage axis, as seen in Fig. 3c,d. The field dependence exhibits the same step-like behaviour as observed in Fig. 3a,b, and for this current direction closely resembles the magnetic hysteresis loop of the Fe detector contact itself. The detector voltage often exhibits a local peak at the coercive field as the contact magnetization reverses, which we tentatively attribute to reversal of magnetic domains in the detector (which is not single domain). The voltage on a non-magnetic detector exhibits no step-like behaviour (see Supplementary Section 'Control experiments').

Transport measurements were also performed with the applied field and detector contact magnetization parallel/antiparallel to the current direction, and these data are summarized in Fig. 3e,f. In this configuration, the TI surface-state spin is now orthogonal to the detector contact magnetization, and a completely different field dependence is observed. No abrupt step-like change or hysteresis in the detector voltage occurs as the applied field is swept through the contact's coercive field and the contact magnetization is reversed. Instead, a smoothly varying voltage is observed, typical of a pseudo-linear magnetoresistance obtained with non-magnetic contacts.

A second set of devices was prepared with Fe/Al_2O_3 tunnel barrier contacts on an 11 nm Bi_2Se_3 epilayer on a sapphire substrate using the contact layout of Fig. 2c. To improve signal quality, a non-magnetic contact immediately adjacent to the ferromagnetic detector was used as the voltage reference to directly subtract non-magnetization-dependent background contributions; this results in a substantial improvement to the signal quality and reduction in the background voltage. An optical image of one of the devices measured is shown in Fig. 4a, and representative data for −0.5 mA bias current are shown in Fig. 4b. The dependence of the Fe detector voltage on the magnetic field and direction of the bias current is the same as described for Fig. 3. Note that even though a smaller unpolarized current is applied, the measured spin voltage is comparable to that for the 45–nm-thick Bi_2Se_3 film of Fig. 3.

The correlation between detector magnetization and current-induced spin polarization of the spin-momentum locked TI surface bands is more easily followed using a ferromagnetic detector metal with a larger coercive field and a skewed magnetic hysteresis loop, so that reversal of the contact magnetization occurs over a larger range of applied field. To this end, a third set of devices was prepared with ferromagnetic contacts consisting of polycrystalline Co films on 2-nm-thick MgO deposited onto a graphene monolayer previously mechanically transferred onto a 23-nm-thick Bi_2Se_3 film. The contact geometry of Fig. 2c was used and the graphene was removed between the contacts.

These data are summarized in Fig. 4c–h. The dependence of the Co detector voltage on the magnetic field and direction of the TI bias current are as described previously, demonstrating that the spin-voltage behaviours measured are reproduced with a completely different detector. The same step-like behaviour in the measured spin voltage is observed as the contact magnetization switches at Co film coercive fields of ±150 Oe for bias currents of +1 and +2 mA (Fig. 4c,e). When the TI bias current is reversed, the spin voltage changes sign (Fig. 4d,f). The larger coercive field of the Co and the slower reversal and saturation of the magnetization are reflected in the width of the hysteretic loop observed in the detector voltage. This is especially evident when the magnetic

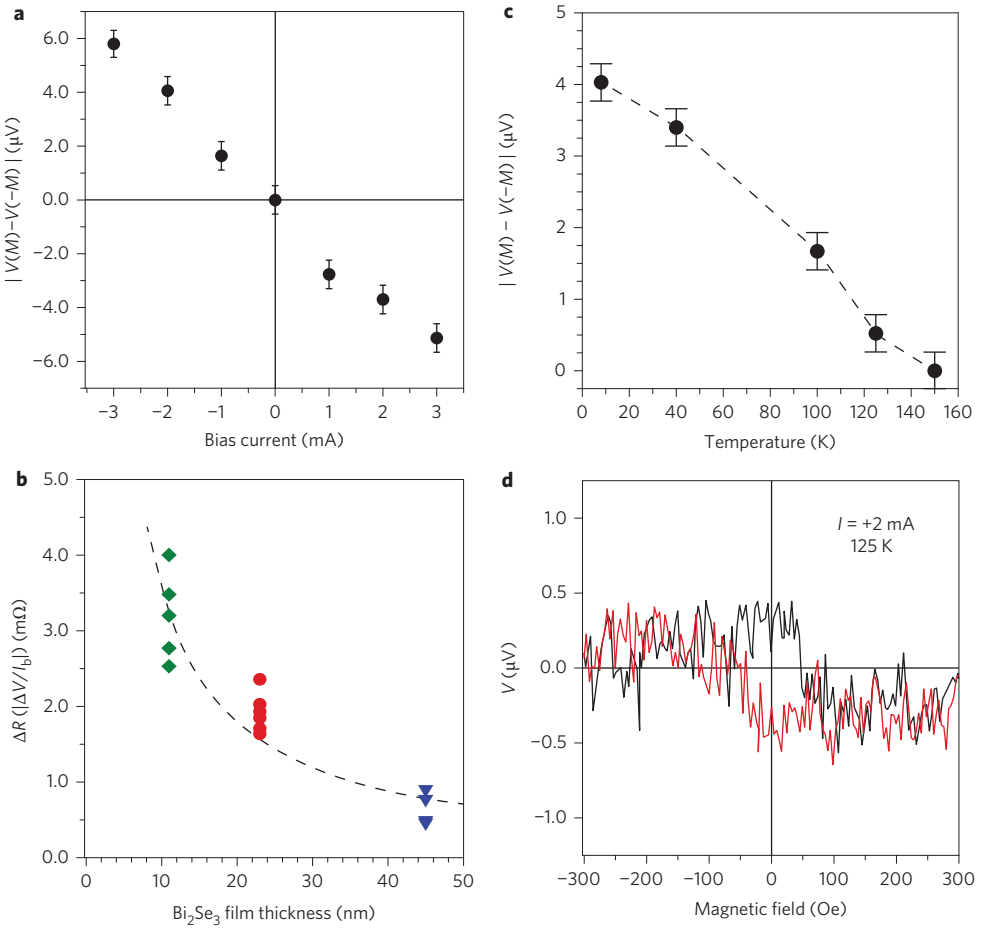

Figure 5 | Dependence of the ferromagnetic detector voltage on bias current, thickness and temperature. a, Height of the voltage hysteresis curve $\Delta V = V(M) - V(-M)$ for applied fields greater than the contact coercive field as a function of bias current for samples with 80 × 80 μm Co/MgO/graphene detector contacts. **b**, $\Delta R = |\Delta V/I_b|$ as a function of the Bi_2Se_3 film thickness, where I_b is the bias current applied through the Bi_2Se_3. Dashed line shows an inverse thickness dependence scaled vertically to fit the data. Each data point corresponds to a different bias current for a device on each of the three Bi_2Se_3 film thicknesses used here. Green diamond and blue triangle symbols are for Bi_2Se_3 films with Fe/Al_2O_3 contacts, while the red circles indicate Bi_2Se_3 films with Co/MgO/graphene contacts. **c**, Height of the voltage hysteresis curve $|\Delta V|$ as a function of temperature for samples with Co/MgO/graphene detector contacts on a 23 nm Bi_2Se_3 film and 2 mA bias current. The detector voltage is measured with the magnetization collinear with the induced TI spin. **d**, Detector voltage versus magnetic field at 125 K for the Co/MgO/graphene/23 nm Bi_2Se_3 film and +2 mA bias current. The black trace corresponds to a positive magnetic field sweep (from negative to positive values) and the red trace corresponds to a negative field sweep. The error bars in panels **a** and **c** represent the uncertainty in determining the height of the voltage hysteresis curve arising from the signal-to-noise ratio and the background.

field is applied along the bias current direction, as shown in Fig. 4g,h. At high applied field, the magnetization is orthogonal to the current-induced spin polarization and the projection of the surface-state spin onto the detector magnetization is zero. As the applied field is reversed, the magnetization rotates through a parallel (or antiparallel) orientation with the spin, producing a small peak in the detector voltage, and then again becomes orthogonal to the induced spin. The linear background evident in Fig. 3e,f, attributed to conventional magnetoresistance, is absent here because the non-magnetic contact adjacent to the detector is used as reference for the voltage measurement.

The change in detector voltage, $\Delta V = V(M) - V(-M)$, measured as the magnetization reverses, increases linearly with bias current I_b flowing in the Bi_2Se_3 film, as shown in Fig. 5a for the Co-based detector data of Fig. 4. The value $|\Delta V/I_b| = \Delta R$ scales inversely with the thickness of the Bi_2Se_3 film (Fig. 5b), demonstrating that the detector voltage measured derives from the TI surface states and not the bulk. The bias current applied between the non-magnetic ohmic contacts is shunted by the bulk and only that fraction flowing in the surface layer contributes to spin momentum locking in the TI surface state to generate a spin voltage. If the sample consists of N quintuple layers (QL, the basic five-atom-layer unit Se-Bi-Se-Bi-Se, ~1 nm thick in this naturally layered compound) and each QL has equal conductivity, then the bias current through the surface layer is $1/N$ and the spin voltage should scale accordingly. This behaviour is clearly observed in Fig. 5b.

These observations for the two ferromagnetic contact structures underscore the reproducibility of the data and the fact that these behaviours are due to bias current-induced spin in the TI Dirac surface states and are independent of the details of the contact itself. The flow of current in the TI surface band induces a net spin polarization aligned in-plane and orthogonal to the current. The strong correlation of the measured ferromagnetic detector voltage with both the amplitude and the relative orientation of the bias current-induced spin to the detector magnetization provide clear and compelling evidence for spin-dependent detection.

This also excludes possible contributions from local Hall effects resulting from perpendicular components of the fringe field at the edges or domain boundaries of the ferromagnetic detector contact, or other Lorentz force-based effects, because any such fringe fields are present regardless of the orientation of the

in-plane magnetization and direction of current flow. The voltages on non-magnetic detector contacts and magnetic ohmic (rather than tunnel barrier) detector contacts show no such field dependent switching (see Supplementary Section 'Control experiments'), excluding contributions from other mechanisms. We also discuss and exclude contributions from anisotropic magnetoresistance and anomalous Hall effects, which might arise from current shunting by the detector contact (see Supplementary Section 'Anisotropic magnetoresistance and anomalous Hall effects; and Additional control experiments'). Thus, the voltage on our ferromagnetic tunnel contact directly reflects the existence and orientation of a current-induced spin polarization of the TI Dirac surface bands.

The hysteretic behaviour of the detector voltage decreases with increasing temperature and disappears by 150 K. The height of the hysteresis curve $|V(M)-V(-M)|$ for applied fields greater than the contact coercive field is plotted as a function of temperature in Fig. 5c. The data at 125 K are shown in Fig. 5d. Spin-resolved photoemission has mapped the Bi_2Se_3 surface states at temperatures as high as 300 K (refs 14,23). This discrepancy may be due to effects induced by the ambient measurement environment used for our work rather than the ultrahigh-vacuum environment required for photoemission, or to mechanisms that are transport specific. Because our samples are strongly n-type ($\sim 1 \times 10^{19}$ cm^{-3}), we tentatively attribute the temperature limit of 150 K to thermal contributions from the bulk that dilute and overwhelm the surface band contribution. A more meaningful assessment of temperature dependence will require better control of the carrier density either by electrostatic gating or improvements in sample fabrication.

The use of a ferromagnetic contact in a multi-terminal configuration to detect a net spin polarization produced in an adjacent non-magnetic medium by some form of spin injection is well established[28] and has been applied to a variety of materials including metals, semiconductors and carbon nanostructures[30,31]. The ferromagnetic contact is typically used as a voltage probe that draws no current (the voltage is proportional to the projection of the spin polarization onto the detector magnetization). Such an approach has been quantitatively treated by Hong and colleagues for the specific case of current-induced spin polarization in a TI in both diffusive and ballistic regimes[29]. They show that the ferromagnetic detector voltages $V(M)$ we measure experimentally (Figs 3 and 4) are directly related to the current-induced spin polarization by $[V(\mathbf{M})-V(-\mathbf{M})] = I_b R_B P_{FM}(\mathbf{p}\cdot\mathbf{M}_u)$, where I_b is the (hole) bias current in the $+x$ direction, R_B is the ballistic resistance of the channel and P_{FM} is the transport spin polarization of the FM detector metal. $\mathbf{M}_u$ is a unit vector along the detector magnetization $\mathbf{M}$, and $\mathbf{p}$ is the degree of spin polarization induced per unit bias current by both spin-momentum locking in TI Dirac surface states[17,18] as well as Rashba spin–orbit coupling. The Dirac surface state and Rashba contributions are opposite in sign.

Our measured values $[V(\mathbf{M})-V(-\mathbf{M})]$ exhibit the essential characteristics expected from this equation: they scale linearly with bias current and exhibit the angular dependence given by $\mathbf{p}\cdot\mathbf{M}_u$. The sign of our measured values $[V(\mathbf{M})-V(-\mathbf{M})]$ indicates that the Dirac surface state contribution dominates, as expected from theory[18] and explicit model calculations[29]. We discuss the sign of the voltage expected for spin-momentum locking and Rashba in the Supplementary Section 'Two dimensional electron gas states and potential Rashba contribution' and show that the Rashba-induced polarization is expected to be small, even for strongly enhanced spin–orbit coupling. The temperature dependence we observe in Fig. 5c is also significantly stronger than that reported for Rashba-induced polarization[32]. A quantitative experimental determination of $\mathbf{p}$ is more elusive, because the bias current has parallel bulk and surface-state conduction paths and only that fraction flowing in the surface channel contributes to the spin polarization arising from Dirac states. We estimate $|\mathbf{p}| \approx 0.2$ from the data of Fig. 4b or e based on the following assumptions: $P_{FM}(\mathrm{Fe, Co}) \approx 0.4$, $k_F \approx 0.15$ A^{-1}, only bias current flowing in a 1-nm-thick surface channel contributes to the spin polarization, and the conductivities of the surface and bulk conduction channels are equal. This value is reasonably consistent with theory[18,29], but subject to the uncertainties in bias current distribution already noted. It represents a lower bound for the polarization produced by spin-momentum locking, because in our highly n-doped samples, E_F lies well above the conduction band-edge and contributions from Rashba spin-split states with opposite net spin polarization will reduce the voltage we measure and the corresponding estimate of TI surface-state polarization (fig. 4 of ref. 29).

In conclusion, the intrinsic sensitivity to spin polarization afforded by a ferromagnetic contact enables one to distinguish the current-induced TI surface band spin polarization from an unpolarized background. The magnitude and temperature dependence of the spin voltage we observe is probably compromised by bulk (non-TI surface) states, which provide a parallel conduction path and a large unpolarized electron background. We anticipate that improvements in Bi_2Se_3 growth will lead to significantly lower unintentional doping levels, reducing parasitic conduction pathways and enhancing the effects we observe. Gating such samples to position E_F between the Dirac point and the bulk conduction band is expected to significantly increase the spin voltage and measured spin polarization and will enable further insight into the behaviour of the TI surface states and spin-momentum locking.

Methods

The growth of Bi_2Se_3 films was carried out on epitaxial graphene/SiC(0001) and Al_2O_3(0001) substrates in an ultrahigh-vacuum (UHV) system (base pressure $\sim 1 \times 10^{-10}$ torr) that integrates two MBE chambers and a low-temperature (5–300 K) scanning tunnelling microscope (STM)[33,34]. As-received nitrogen-doped 6H-SiC(0001) substrates were first etched in a H_2/Ar atmosphere in a separate chamber at <1,500 °C to remove polishing damage. They were then transferred to the MBE system and annealed in UHV in a Si flux (<0.1 monolayers min^{-1}) at 950 °C to produce a (3 × 3) reconstructed surface and further annealed at temperatures of 1000–1300 °C without Si flux to grow epitaxial graphene[35]. For the growth of Bi_2Se_3, the substrate was held at 275–325 °C and Bi and Se were supplied via separate Knudsen cells at 460 and 250 °C, respectively. For Bi_2Se_3 growth on Al_2O_3(0001) substrates, a two-step process was used[36]: 2–3 QL of Bi_2Se_3 were first deposited at a reduced temperature of 100 °C and the substrate temperature was then slowly raised to 300 °C where the rest of the film was deposited. *In situ* STM imaging was used to monitor the surface morphology and electronic structure and to ensure optimal layer-by-layer spiral growth. The as-grown film exhibited a Dirac point 250 meV below the Fermi level in tunnelling spectra, indicating the n-type doping typically seen in MBE-grown materials due to Se vacancies. The character of the topologically protected surface states has been shown to be insensitive to morphological defects such as grain boundaries[34].

Two types of ferromagnetic detector contacts were used as spin-sensitive probes. Such contacts have successfully enabled electrical detection of spin current and accumulation in both semiconductors and metals[28,30,37–42].

Fe/Al_2O_3 contacts were formed on the air-exposed surface of 11-nm- and 45-nm-thick Bi_2Se_3 films in a separate MBE system as follows[39]. A 0.7 nm layer of polycrystalline Al was first deposited by MBE and then oxidized in 200 torr O_2 for 20 min in the presence of ultraviolet light in the load-lock chamber. This step was then repeated for a total Al_2O_3 thickness of 2 nm. The sample was then transferred under UHV to an interconnected metals MBE chamber, where 20 nm of polycrystalline Fe was deposited at room temperature from a Knudsen cell. An oxide tunnel barrier was used to prevent potential direct magnetic exchange with the TI surface states, interdiffusion (which may result in undesirable alloy formation and spin scattering) and to better sample the TI surface state at the interface rather than the bulk. The samples were processed into the device structures illustrated in Fig. 2 to enable transport measurements. Standard photolithography and chemical etching methods were used to define the Fe contacts, which ranged in size from 10 × 10 μm^2 to 80 × 80 μm^2, with adjacent contact separation ranging from 45 to 200 μm. Ion milling was used to pattern the Bi_2Se_3 mesa. Large Ti/Au contacts were deposited by liftoff in an electron-beam evaporator as non-magnetic reference contacts and bias current leads. The Fe contacts were capped with 10 nm Ti/100 nm Au, and bond pads for wire-bonded electrical connections were electrically isolated from the substrate using 100 nm of Si_3N_4.

Another set of samples were prepared with Co/MgO/graphene as the ferromagnetic detector contacts on a 23-nm-thick Bi_2Se_3 film. We have previously shown that single-layer graphene forms an effective tunnel barrier on both metal[41] and semiconductor[42] surfaces, which prevents oxidation and interdiffusion[43]. A

single graphene layer grown by chemical vapour deposition[44] was transferred onto the air-exposed Bi_2Se_3 surface and then patterned so that it was only located under the detector contacts (both magnetic and non-magnetic). A 2 nm MgO film was then deposited by electron-beam evaporation following the deposition of a 0.1 nm Ti seed layer. A 15 nm Co layer was immediately deposited in the same evaporation system without breaking vacuum. Similar photolithography steps as described above were used to produce the device structures illustrated in Fig. 2, with adjacent rows of magnetic and non-magnetic (reference) detector contacts. Separate magnetometry measurements confirmed that the ferromagnetic contact magnetization lay in-plane with square hysteresis loops for the Fe and slightly rounded loops for the Co, as expected for these 15- to 20-nm-thick films and their respective magnetocrystalline anisotropies. The contact resistances of the Au/Ti reference and magnetic detector contacts were $\sim$10 Ω and 10^3–10^4 Ω, respectively.

Transport measurements were performed in a closed-cycle cryostat equipped with an electromagnet (4–300 K, ±1,000 Oe). A bias current of 0.5 to 3 mA was applied through a pair of contacts on either side of and collinear with a selected detector contact, and the voltage on the detector contact was recorded as a function of the in-plane magnetic field applied either parallel or orthogonal to the electron bias current direction in the TI.

Received 25 June 2013; accepted 17 January 2014; published online 23 February 2014

References

1. Moore, J. E. The birth of topological insulators. *Nature* **464,** 194–198 (2010).
2. Hasan, M. Z. & Kane, C. L. Colloquium: topological insulators. *Rev. Mod. Phys.* **82,** 3045–3067 (2010).
3. Fu, L., Kane, C. L. & Mele, E. J. Topological insulators in three dimensions. *Phys. Rev. Lett.* **98,** 106803 (2007).
4. Hsieh, D. *et al.* A topological Dirac insulator in a quantum spin Hall phase. *Nature* **452,** 970–975 (2008).
5. Kong, D. & Cui, Y. Opportunities in chemistry and materials science for topological insulators and their nanostructures. *Nature Chem.* **3,** 845–849 (2011).
6. Zutic, I., Fabian, J. & Das Sarma, S. Spintronics: fundamentals and applications. *Rev. Mod. Phys.* **76,** 323–410 (2004).
7. Dery, H., Dalal, P., Cywinski, L. & Sham, L. J. Spin-based logic in semiconductors for reconfigurable large-scale circuits. *Nature* **447,** 573–576 (2007).
8. Pesin, D. & MacDonald, A. H. Spintronics and pseudospintronics in graphene and topological insulators. *Nature Mater.* **11,** 409–416 (2012).
9. Nayak, C. *et al.* Non-abelian anyons and topological quantum computation. *Rev. Mod. Phys.* **80,** 1083–1159 (2008).
10. Fu, L. & Kane, C. L. Superconducting proximity effect and Majorana fermions at the surface of a topological insulator. *Phys. Rev. Lett.* **100,** 096407 (2008).
11. Qi, X-L., Li, R., Zang, J. & Zhang, S-C. Inducing a magnetic monopole with topological surface states. *Science* **323,** 1184–1187 (2009).
12. Qi, X-L., Hughes, T. L. & Zhang, S-C. Topological field theory of time-reversal invariant insulators. *Phys. Rev. B* **78,** 195424 (2008).
13. Zhang, H. *et al.* Topological insulators in Bi_2Se_3, Bi_2Te_3 and Sb_2Te_3 with a single Dirac cone on the surface. *Nature Phys.* **5,** 438–442 (2009).
14. Hsieh, D. *et al.* A tunable topological insulator in the spin helical Dirac transport regime. *Nature* **460,** 1101–1105 (2009).
15. Chen, Y. L. *et al.* Experimental realization of a three-dimensional topological insulator, Bi_2Te_3. *Science* **325,** 178–181 (2009).
16. Burkov, A. A. & Hawthorn, D. G. Spin and charge transport on the surface of a topological insulator. *Phys. Rev. Lett.* **105,** 066802 (2010).
17. Culcer, D., Hwang, E. H., Stanescu, T. D. & Das Sarma, S. Two-dimensional surface charge transport in topological insulators. *Phys. Rev. B* **82,** 155457 (2010).
18. Yazyev, V., Moore, J. E. & Louie, S. G. Spin polarization and transport of surface states in the topological insulators Bi_2Se_3 and Bi_2Te_3 from first principles. *Phys. Rev. Lett.* **105,** 266806 (2010).
19. Kuroda, K. *et al.* Hexagonally deformed Fermi surface of the 3D topological insulator Bi_2Se_3. *Phys. Rev. Lett.* **105,** 076802 (2010).
20. Souma, S. *et al.* Direct measurement of the out-of-plane spin texture in the Dirac-cone surface state of a topological insulator. *Phys. Rev. Lett.* **106,** 216803 (2011).
21. Pan, Z-H. *et al.* Electronic structure of the topological insulator Bi_2Se_3 using angle-resolved photoemission spectroscopy: evidence for a nearly full surface spin polarization. *Phys. Rev. Lett.* **106,** 257004 (2011).
22. McIver, J. W., Hsieh, D., Steinberg, H., Jarillo-Herrero, P. & Gedik, N. Control over topological insulator photocurrents with light polarization. *Nature Nanotech.* **7,** 96–100 (2012).
23. Pan, Z-H. *et al.* Measurement of an exceptionally weak electron–phonon coupling on the surfaces of the toplogical insulator Bi_2Se_3 using angle-resolved photoemission. *Phys. Rev. Lett.* **108,** 187001 (2012).
24. Valla, T., Pan, Z-H., Gardner, D., Lee, Y. S. & Chu, S. Photoemission spectroscopy of magnetic and nonmagnetic impurities on the surface of the Bi_2Se_3 topological insulator. *Phys. Rev. Lett.* **108,** 117601 (2012).
25. Scholz, M. R. *et al.* Tolerance of topological surface states towards magnetic moments: Fe on Bi_2Se_3. *Phys. Rev. Lett.* **108,** 256810 (2012).
26. Ji, H. *et al.* Bulk intergrowth of a topological insulator with a room temperature ferromagnet. *Phys. Rev. B* **85,** 165313 (2012).
27. Xu, S-Y. *et al.* Hedgehog spin texture and Berry's phase tuning in a magnetic topological insulator. *Nature Phys.* **8,** 616–622 (2012).
28. Silsbee, R. H. Spin–orbit induced coupling of charge current and spin polarization. *J. Phys. Condens. Matter* **16,** R179–R207 (2004).
29. Hong, S., Diep, V., Datta, S. & Chen, Y. P. Modeling potentiometric measurements in topological insulators including parallel channels. *Phys. Rev. B* **86,** 085131 (2012).
30. Lou, X. *et al.* Electrical detection of spin transport in lateral ferromagnet–semiconductor devices. *Nature Phys.* **3,** 197–202 (2007).
31. Tombros, N., Jozsa, C., Popinciuc, M., Jonkman, H. T. & van Wees, B. J. Electronic spin transport and spin precession in single graphene layers at room temperature. *Nature* **448,** 571–574 (2007).
32. Hammar, P. R. & Johnson, M. Spin-dependent current transmission across a ferromagnet-insulator-two-dimensional electron gas junction. *Appl. Phys. Lett.* **79,** 2591–2593 (2001).
33. Liu, Y., Weinert, M. & Li, L. Spiral growth without dislocations: molecular beam epitaxy of the topological insulator Bi_2Se_3 on epitaxial graphene/SiC(0001). *Phys. Rev. Lett.* **108,** 115501 (2012).
34. Liu, Y. *et al.* Charging Dirac states at anti-phase domain boundaries in the three-dimensional topological insulator Bi_2Se_3. *Phys. Rev. Lett.* **110,** 186804 (2013).
35. Qi, Y., Rhim, S. H., Sun, G. F., Weinert, M. & Li, L. Epitaxial graphene on SiC(0001): more than just honeycombs. *Phys. Rev. Lett.* **105,** 085502 (2010).
36. Li, H. D. *et al.* The van der Waals epitaxy of Bi_2Se_3 on the vicinal Si(111) surface: an approach for preparing high-quality thin films of a topological insulator. *New J. Phys.* **12,** 103038 (2010).
37. Johnson, M. & Silsbee, R. H. Interfacial charge-spin coupling: injection and detection of spin magnetization in metals. *Phys. Rev. Lett.* **55,** 1790–1793 (1985).
38. Jedema, F. J., Heersche, H. B., Filip, A. T., Baselmans, J. J. A. & van Wees, B. J. Electrical detection of spin precession in a metallic mesoscopic spin valve. *Nature* **416,** 713–716 (2002).
39. Van 't Erve, O. M. J. *et al.* Electrical injection and detection of spin-polarized carriers in silicon in a lateral transport geometry. *Appl. Phys. Lett.* **91,** 212109 (2007).
40. Sasaki, T. *et al.* Electrical spin injection into silicon using MgO tunnel barrier. *Appl. Phys. Express* **2,** 053003 (2009).
41. Cobas, E., Friedman, A. L., van 't Erve, O. M. J., Robinson, J. T. & Jonker, B. T. Graphene as a tunnel barrier: graphene-based magnetic tunnel junctions. *Nano Lett.* **12,** 3000–3004 (2012).
42. Van 't Erve, O. M. J. *et al.* Low-resistance spin injection into silicon using graphene tunnel barriers. *Nature Nanotech.* **7,** 737–742 (2012).
43. Chen, S. *et al.* Oxidation resistance of graphene-coated Cu and Cu/Ni alloy. *ACS Nano* **5,** 1321–1327 (2011).
44. Li, X. *et al.* Large-area graphene single crystals grown by low-pressure chemical vapor deposition of methane on copper. *J. Am. Chem. Soc.* **133,** 2816–2819 (2011).

Acknowledgements

The authors acknowledge support for this work from core programmes at the Naval Research Laboratory, and the Office of Naval Research contract N0001413WX21513.

Author contributions

C.H.L., L.L. and B.T.J. conceived and designed the experiments. Y.L. and L.L. grew the Bi_2Se_3 films. J.T.R. provided the large-area graphene. C.H.L. fabricated the devices and performed the transport measurements with assistance from O.M.J.E. C.H.L., O.M.J.E. and B.T.J. analysed the data. B.T.J. and C.H.L. wrote the paper. All authors discussed the results and commented on the manuscript.

Additional information

Supplementary information is available in the online version of the paper. Reprints and permissions information is available online at www.nature.com/reprints. Correspondence and requests for materials should be addressed to C.H.L. and B.T.J.

Competing financial interests

The authors declare no competing financial interests.